Research Article Vol. 25, No. 24 | 27 Nov 2017 | OPTICS EXPRESS 29798

49.6 Gb/s direct detection DMT transmission over 40 km single mode fibre using an electrically packaged silicon photonic modulator

C. Lacava,[1,*] I. Cardea,[1,2] I. Demirtzioglou,[1] A.E. Khoja, [1] Li Ke,[1] D. J. Thomson,[1] X. Ruan,[3] F. Zhang,[3] G.T. Reed,[1] D.J. Richardson,[1] and P. Petropoulos[1]

[1] *Optoelectronics Research Centre, University of Southampton SO17 1BJ Southampton, UK*
[2] *Currently with Photonic Systems Laboratory, EPFL CH-1015 Lausanne, Switzerland*
[3] *State Key Laboratory of Advanced Optical Communication Systems and Networks, Peking University, Beijing, China*
[*] *C.Lacava@soton.ac.uk*

Abstract: We present the characterization of a silicon Mach-Zehnder modulator with electrical packaging and show that it exhibits a large third-order intermodulation spurious-free dynamic range ($> 100\ dB\ Hz^{2/3}$). This characteristic renders the modulator particularly suitable for the generation of high spectral efficiency discrete multi-tone signals and we experimentally demonstrate a single-channel, direct detection transmission system operating at 49.6 Gb/s, exhibiting a baseband spectral efficiency of 5 b/s/Hz. Successful transmission is demonstrated over various lengths of single mode fibre up to 40 km, without the need of any amplification or dispersion compensation.

OCIS codes: (060.0060) Fiber optics and optical communications; (130.0250) Optoelectronics; (250.5300) Photonic integrated circuits; (250.4110) Modulators.

References and links

1. C. Kachris, K. Kanonakis, and I. Tomkos, "Optical interconnection networks in data centers: recent trends and future challenges," IEEE Commun. Mag. **51**, 39–45 (2013).
2. C. R. Doerr, "Silicon photonic integration in telecommunications," Front. Phys. **3**, 1–16 (2015).
3. B. Jalali and F. Sasan, "Silicon photonics," J. Lightw. Technol. **24**, 4600–4615 (2004).
4. A. Rickman, "The commercialization of silicon photonics," Nat. Photonics **8**, 579–582 (2014).
5. G. T. Reed, G. Mashanovich, F. Y. Gardes, and D. J. Thomson, "Silicon optical modulators," Nat. Photonics **4**, 518–526 (2010).
6. D. Patel, A. Samani, V. Veerasubramanian, S. Ghosh, and D. V. Plant, "Silicon photonic segmented modulator-based electro-optic DAC for 100 Gb/s PAM-4 generation," IEEE Photon. Technol. Lett. **27**, 2433–2436 (2015).
7. C. Lacava, Z. Liu, D. Thomson, L. Ke, J. M. Fedeli, D. J. Richardson, G. T. Reed, and P. Petropoulos, "Silicon photonic Mach Zehnder modulators for next-generation short-reach optical communication networks," (2016), vol. 9772, p. 977209.
8. T. Pinguet, B. Analui, E. Balmater, D. Guckenberger, M. Harrison, R. Koumans, D. Kucharski, Y. Liang, G. Masini, A. Mekis, S. Mirsaidi, A. Narasimha, M. Peterson, D. Rines, V. Sadagopan, S. Sahni, T. J. Sleboda, D. Song, Y. Wang, B. Welch, J. Witzens, J. Yao, S. Abdalla, S. Gloeckner, P. De Dobbelaere, and G. Capellini, "Monolithically integrated high-speed CMOS photonic transceivers," in "2008 5th International Conference on Group IV Photonics, GFP," , vol. 1 (2008), vol. 1, pp. 362–364.
9. B. Analui, D. Guckenberger, D. Kucharski, and A. Narasimha, "A fully integrated 20-Gb/s optoelectronic transceiver implemented in a standard 0.13-nm CMOS SOI technology," IEEE Solid State Circuits Mag. **41**, 2945–2955 (2006).
10. C. Li, R. Bai, A. Shafik, E. Z. Tabasy, G. Tang, C. Ma, C. H. Chen, Z. Peng, M. Fiorentino, P. Chiang, and S. Palermo, "A ring-resonator-based silicon photonics transceiver with bias-based wavelength stabilization and adaptive-power-sensitivity receiver," in "Digest of Technical Papers - IEEE International Solid-State Circuits Conference," , vol. 56 (2013), vol. 56, pp. 124–125.

#308048 https://doi.org/10.1364/OE.25.029798
Journal © 2017 Received 4 Oct 2017; revised 2 Nov 2017; accepted 3 Nov 2017; published 14 Nov 2017

11. A. Narasimha, B. Analui, Y. Liang, T. J. Sleboda, S. Abdalla, E. Balmater, S. Gloeckner, D. Guckenberger, M. Harrison, R. G. M. P. Koumans, D. Kucharski, A. Mekis, S. Mirsaidi, D. Song, and T. Pinguet, "A fully integrated 4x 10-Gb/s DWDM optoelectronic transceiver implemented in a standard 0.13 um CMOS SOI technology," IEEE Solid State Circuits Mag. **42**, 2736–2744 (2007).
12. L. Chen and M. Lipson, "Ultra-low capacitance and high speed germanium photodetectors on silicon," Opt. Express **17**, 7901–7906 (2009).
13. L. Vivien, J. Osmond, J.-M. Fédéli, D. Marris-Morini, P. Crozat, J.-F. Damlencourt, E. Cassan, Y. Lecunff, and S. Laval, "42 GHz pin Germanium photodetector integrated in a silicon-on-insulator waveguide," Opt. Express **17**, 6252 (2009).
14. S. Famà, L. Colace, G. Masini, G. Assanto, and H. C. Luan, "High performance germanium-on-silicon detectors for optical communications," Appl. Phys. Lett. **81**, 586–588 (2002).
15. P. Dong, Y.-K. Chen, G.-H. Duan, and D. T. Neilson, "Silicon photonic devices and integrated circuits," Nanophotonics **3**, 215–228 (2014).
16. M. Poulin, C. Latrasse, J. Gagné, Y. Painchaud, M. Cyr, and C. Paquet, "100 Gb/s PAM-4 transmission over 1.5 km using a SiP series push-pull modulator at 1310 nm," in "European Conference on Optical Communication 2014," (2014), 1, pp. 5–7.
17. P. Winzer and R.-J. Essiambre, "Advanced optical modulation formats," Proceedings of the IEEE **94**, 952–985 (2006).
18. P. Dong, J. Lee, Y.-k. Chen, L. L. Buhl, S. Chandrasekhar, J. H. Sinsky, and K. Kim, "Four-channel 100-Gb/s per channel discrete multitone modulation using silicon photonic integrated circuits," J. Lightw. Technol. **34**, 79–84 (2016).
19. X. Wu, C. Huang, K. Xu, C. Shu, S. Member, H. K. Tsang, and S. Member, "128-Gb/s line rate OFDM signal modulation using an integrated silicon microring modulator," IEEE Photon. Technol. Lett. **28**, 2058–2061 (2016).
20. C. Y. Wong, S. Zhang, Y. Fang, L. Liu, T. Wang, Q. Zhang, S. Deng, G. N. Liu, and X. Xu, "Silicon IQ modulator for next-generation metro network," J. Lightw. Technol. **34**, 730–736 (2016).
21. Y. Kai, M. Nishihara, T. Tanaka, R. Okabe, T. Takahara, and J. C. Rasmussen, "130-Gbps DMT transmission using silicon Mach-Zehnder modulator with chirp control at 1.55 um," in "Optical Fiber Communication Conference 2015," (2015), p. Th4A.1.
22. R. Xiaoke, K. Li, D. J. Thomson, C. Lacava, F. Meng, I. Demirtzioglou, P. Petropoulos, Y. Zhu, G. T. Reed, and F. Zhang, "Experimental comparison of direct detection Nyquist SSB transmission based on silicon dual-drive and IQ Mach-Zehnder modulators with electrical packaging," Opt. Express **25**, 19332–19342 (2017).
23. M. Chagnon, M. Osman, M. Poulin, C. Latrasse, J.-F. Gagné, Y. Painchaud, C. Paquet, S. Lessard, and D. Plant, "Experimental study of 112 Gb/s short reach transmission employing PAM formats and SiP intensity modulator at 13 μm," Opt. Express **22**, 21018 (2014).
24. D. J. Thomson, F. Y. Gardes, J.-M. Fedeli, S. Zlatanovic, Y. Hu, B. P. P. Kuo, E. Myslivets, N. Alic, S. Radic, G. Z. Mashanovich, and G. T. Reed, "50-Gb/s Silicon Optical Modulator," IEEE Photon. Technol. Lett. **24**, 234–236 (2012).
25. G. T. Reed, G. Z. Mashanovich, F. Y. Gardes, M. Nedeljkovic, Y. Hu, D. J. Thomson, K. Li, P. R. Wilson, S.-W. Chen, and S. S. Hsu, "Recent breakthroughs in carrier depletion based silicon optical modulators," Nanophotonics **3**, 229–245 (2014).
26. R. A. Soref and B. R. Bennett, "Electrooptical effects in silicon," IEEE J. Quantum Electron. **23**, 123–129 (1987).
27. J. Ding, S. Shao, L. Zhang, X. Fu, and L. Yang, "Method to improve the linearity of the silicon Mach-Zehnder optical modulator by doping control," Opt. Express **24**, 24641 (2016).
28. H. Yu, M. Pantouvaki, J. Van Campenhout, D. Korn, K. Komorowska, P. Dumon, Y. Li, P. Verheyen, P. Absil, L. Alloatti, D. Hillerkuss, J. Leuthold, R. Baets, and W. Bogaerts, "Performance tradeoff between lateral and interdigitated doping patterns for high speed carrier-depletion based silicon modulators," Opt. Express **20**, 12926 (2012).
29. T. Y. Liow, K. W. Ang, Q. Fang, J. F. Song, Y. Z. Xiong, M. B. Yu, G. Q. Lo, and D. L. Kwong, "Silicon modulators and germanium photodetectors on SOI: Monolithic integration, compatibility, and performance optimization," IEEE J. Sel. Topics Quantum Electron. **16**, 307–315 (2010).
30. N. N. Feng, S. R. Liao, D. Z. Feng, P. Dong, D. W. Zheng, H. Liang, R. Shafiiha, G. L. Li, J. E. Cunningham, A. V. Krishnamoorthy, and M. Asghari, "High speed carrier-depletion modulators with 1.4V-cm V pi L integrated on 0.25 um silicon-on-insulator waveguides," Opt. Express **18**, 7994–7999 (2010).
31. H. Yang, S. C. J. Lee, E. Tangdiongga, C. Okonkwo, H. P. A. Van Den Boom, F. Breyer, S. Randel, and A. M. J. Koonen, "47.4 Gb/s transmission over 100 m graded-index plastic optical fiber based on rate-adaptive discrete multitone modulation," J. Lightw. Technol. **28**, 352–359 (2010).
32. I. Neokosmidis, T. Kamalakis, J. W. Walewski, B. Inan, and T. Sphicopoulos, "Impact of nonlinear LED transfer function on discrete multitone modulation: analytical approach," J. Lightw. Technol. **27**, 4970–4978 (2009).
33. A. Khilo, C. M. Sorace, and F. X. Kärtner, "Broadband linearized silicon modulator," Opt. Express **19**, 4485–4500 (2011).
34. S. Zhou, L. Xiang, Y. Lilin, Y. Qi, and F. Songnian, "Transmission of 2 x 56 Gb/s PAM-4 signal over 100 km SSMF using 18 GHz DMLs," Opt. Lett. **41**, 1805–1808 (2016).
35. D. a. Marpaung, "High dynamic range analog photonic links: design and implementation," Ph.D. thesis, University

of Twente, The Netherlands (2009).
36. B. H. Kolner and D. W. Dolfi, "Intermodulation distortion and compression in an integrated electrooptic modulator," Appl. Optics **26**, 3676–3680 (1987).
37. A. Ayazi, T. Baehr-Jones, Y. Liu, A. E.-J. Lim, and M. Hochberg, "Linearity of silicon ring modulators for analog optical links," Opt. Express **20**, 13115 (2012).
38. J. Cardenas, P. A. Morton, J. B. Khurgin, A. Griffith, C. B. Poitras, K. Preston, and M. Lipson, "Linearized silicon modulator based on a ring assisted Mach Zehnder inteferometer," Opt. Express **21**, 22549–22557 (2013).
39. A. M. Gutierrez, J. V. Galan, J. Herrera, A. Brimont, D. Marris-Morini, J. M. Fédéli, L. Vivien, and P. Sanchis, "High linear ring-assisted MZI electro-optic silicon modulators suitable for radio-over-fiber applications," IEEE International Conference on Group IV Photonics GFP **4**, 57–59 (2012).
40. C. Zhang, P. Morton, J. B. Khurgin, J. D. Peters, and J. Bowers, "Ultralinear heterogeneously integrated ring-assisted Mach Zehnder interferometer modulator on silicon," Optica **3**, 1–6 (2016).
41. X. Luo, X. Tu, J. Song, L. Ding, Q. Fang, T.-Y. Liow, M. Yu, and G.-Q. Lo, "Slope efficiency and spurious-free dynamic range of silicon Mach-Zehnder modulator upon carrier depletion and injection effects," Opt. Express **21**, 16570 (2013).
42. M. Streshinsky, A. Ayazi, Z. Xuan, A. E.-J. Lim, G.-Q. Lo, T. Baehr-Jones, and M. Hochberg, "Highly linear silicon traveling wave Mach-Zehnder carrier depletion modulator based on differential drive," Opt. Express **21**, 3818–3825 (2013).
43. J. M. Cioffi, "Multi-channel modulation," in "Stanford online repository," (2002), December, pp. 305–330.
44. S. C. Lee, F. Breyer, S. Randel, R. Gaudino, G. Bosco, A. Bluschke, M. Matthews, P. Rietzsch, R. Steglich, H. P. van den Boom, and A. M. Koonen, "Discrete multitone modulation for maximizing transmission rate in step-index plastic optical fibers," J. Lightw. Technol. **27**, 1503–1513 (2009).
45. U. Gliese, S. Norskov, and T. N. Nielsen, "Chromatic dispersion in fibre-optic microwave and millimiter-wave links," IEEE Trans. Microw. Theory Techn. **44**, 1716–1924 (1996).
46. H. Schmuck, "Comparison of optical millimetre-wave system concepts with regard to chromatic dispersion," Electron. Lett. **31**, 1848–1849 (1995).
47. R. P. Tatam and D. A. Jackson, "Interferometric chromatic dispersion measurements on short lengths of monomode optical fiber," J. Lightw. Technol. **7**, 703–716 (1989).
48. Li Rui, D. Patel, E. El-Fiky, A. Samani, X. Zhenping, M. Osman, and D. V. Plant, "High-speed low-chirp PAM-4 transmission based on push-pull silicon photonic microring modulators," Opt. Express **25**, 13222–13229 (2017).
49. Z. Liu, M. S. Erk, B. Kelly, J. O. Carroll, R. Phelan, B. Thomsen, R. Killey, D. J. Richardson, P. Bayvel, and R. Slavik, "49 Gbit / s direct-modulation and direct-detection transmission over 80 km SMF-28 without optical amplification or filtering," in "European Conference on Optical Communication 2016," (2016), pp. 145–147.
50. P. Dong, X. Chen, K. Kim, S. Chandrasekhar, Y.-K. Chen, and J. H. Sinsky, "128-Gb/s 100-km transmission with direct detection using silicon photonic Stokes vector receiver and I/Q modulator," Opt. Express **24**, 14208 (2016).

---

1. Introduction

The amount of data exchanged over the internet has been growing continuously over the last 20 years, posing new challenges to the global network infrastructure. Data-centers are required to manage increased numbers of connections and services, relating for example to cloud applications or high definition video streaming, and need to be equipped with a new class of cost-effective, wideband, short-to-medium haul interconnections [1]. Recently, silicon photonic-based optical links have been identified as good candidates for intra-data-center communications [2–4] and numerous devices including modulators [5–7], transceivers with electronic integration [8–11], detectors [12–14] and wavelength division multiplexing (WDM) devices [15] have been demonstrated, showing both short- and long-haul transmission capabilities, with single-channel connection speeds that exceed 100 Gb/s [6, 16]. The implementation of short-reach intra-data center links needs to be relatively simple and cost-effective. Direct-detection (DD), unrepeatered and uncompensated transmission is therefore highly desirable in such environments. In this context, advanced modulation formats have shown a great potential as they allow connections with extremely high spectral efficiencies [17], which in turn relax the electrical and optical bandwidth requirements and cost. Both multilevel and multicarrier modulation schemes have recently been demonstrated based on silicon photonic components [16, 18–20], showing that speeds exceeding 100 Gb/s per single channel can be achieved by employing 20-G-class silicon intensity modulators. Among the proposed solutions, discrete multi-tone (DMT) modulation offers the capability to adapt the signal to the channel spectral response, allowing the demonstration of extremely high spectral efficiency transmission [18, 21]. Although 100 Gb/s connections with silicon photonic modulators were demonstrated in [18, 21], the transmission lengths over single mode fibre (SMF) were limited to just 10 km, mainly because of the dispersion power fading effect that becomes an important consideration as the fibre reach increases. Many solutions have been proposed to overcome this limitation, including the adoption of single sideband (SSB) [22] or vestigial sideband (VSB) modulations [18], which however, may significantly increase the hardware complexity. Alternatively, transmission in the O-band has also been considered, however this introduces excess-loss induced optical signal-to-noise ratio penalties [23].

In this paper, we discuss the design and characterization of an electrically-packaged silicon Mach-Zehnder intensity modulator (MZM) that shows a highly linear response. We use this device to demonstrate a 40 km-long DD-DMT link, operating at 49.6 Gb/s, exhibiting an unprecedented baseband spectral efficiency of 5 b/s/Hz, with no need for any amplification or chromatic dispersion compensation. This work shows that cost effective 10G-class silicon photonic modulators can be employed to design 50 Gb/s short-to-medium reach DD optical links, making them a suitable transmitter technology for the optical wiring of next generation data-centers.

2. Device design and characterization

2.1. *MZM design principles*

The device used in the experiments was an unbalanced MZM. The input light was split onto two arms with a 50:50 ratio by means of a multi-mode interference coupler (MMI). Two identical 1.8-mm long phase shifters were placed on each arm (see Fig. 1), constituted of p-n junctions

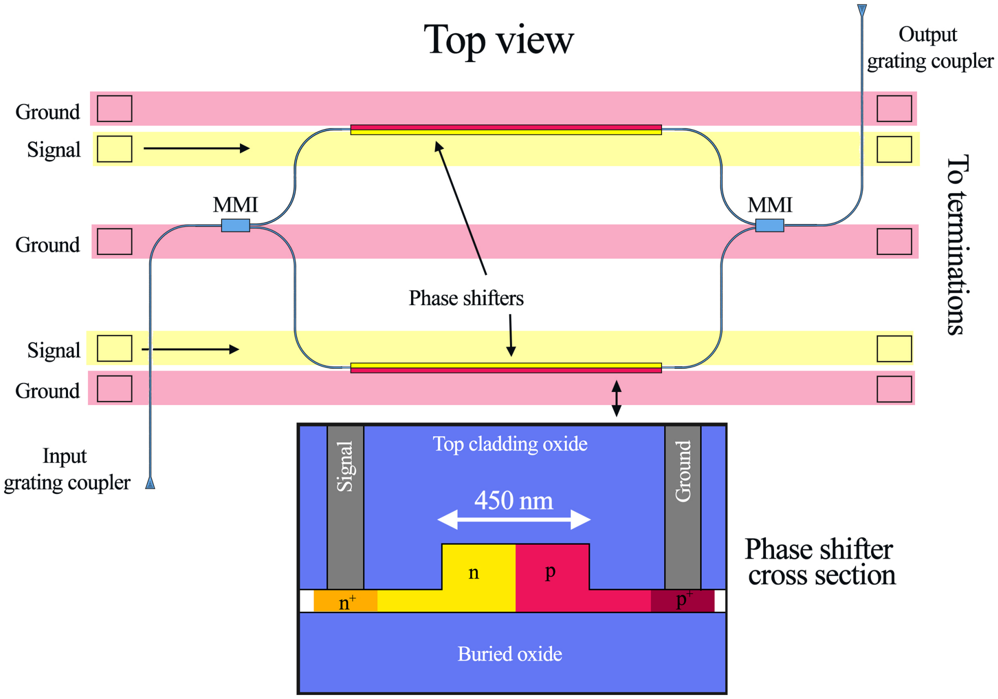

Fig. 1. MZM layout. Inset: phase shifter cross section. The length of each phase shifter is 1.8 mm, while the unbalance between the two MZI paths is equal to 0.18 mm.

connected to coplanar traveling wave electrodes that allowed the carrier density across the silicon waveguide to be modified through the carrier depletion effect [24, 25]. The two paths were subsequently recombined in a second MMI. Two grating couplers were placed at the input and the output end to allow coupling from/to external optical fibres. A coupling loss of 3.5 dB/grating was measured by means of the cut-back technique. The optical sample was surface-mounted on a Printed Circuit Board (PCB). Differential electrical signals were coupled onto the PCB via two SMK connectors and micro-strip lines routed these signals to the input side of the MZM. On the output side, wire bonds were used to connect the differential signals to the PCB, on which the on-board 50 Ω termination was built (see Fig. 1 and Fig. 2).

A reverse voltage applied on the phase shifters induced a carrier concentration distribution change, which in turn caused a material refractive index change through the plasma dispersion effect, according to the following equation [26]:

$$\Delta n(x,y) = \Delta n_e + \Delta n_h = -[8.8x10^{-22}\Delta N + 8.5x10^{-18}(\Delta P)^{0.8}] \tag{1}$$

The waveguide effective refractive index change, can be determined by the overlap integral, between the concentration distribution change and the optical field distribution (determined by the waveguide configuration). Δn_{eff} is expressed as:

$$\Delta n_{eff} = \frac{1}{n_{eff}^{(0)}} \frac{\int\int n(x,y) n^{(0)}(x,y)|E^0(x,y)^2|dxdy}{\int\int |E^{(0)}(x,y)|^2 dxdy} \tag{2}$$

where $n_{eff}^0$is the original waveguide effective refractive index when no voltage is applied to the junction and $E_{x,y}^0$ is the spatial distribution of the electrical field of the optical mode in the rib waveguide. In the design stage, we used the commercial software *Silvaco* to calculate the carrier distribution change which was converted to refractive index change with the use of Eq. 1. The optical mode distribution was calculated using a *Matlab* based solver. These results where then combined, making use of Eq. 2 to obtain the effective refractive index difference, as a function of the applied voltage. Our design aimed at the simultaneous optimization of three main parameters: *(i)* modulator loss (mainly influenced by the junction doping level), *(ii)* modulation efficiency and *(iii)* modulation linearity (i.e. third-order inter-modulation distortions, spurious free dynamic range ($SFDR_{IMD_3}$)). The phase shifter section loss coefficient and the efficiency parameter, were derived from the optical simulations (performed by using a *Matlab* solver), while the theoretical inter-modulation distortion, $SFDR_{IMD_3}$, was calculated by numerically modeling the MZM device, as follows: The MZM modulator transfer function can be described by the following equation:

$$P_{out} = P_{in}cos^2\left(\frac{\Delta\phi}{2}\right) = P_{in}cos^2\left(\frac{2\pi L}{\lambda}\Delta n_{eff}(V)\right) \tag{3}$$

where L is the phase shifter length and V the applied voltage. To measure the third-order inter-modulation distortion generated by the device, a two-tones approach was used, where two tones, at different frequencies (ω_1 and ω_2), were used to drive the MZM. The total voltage applied to the device is

$$V = V_{DC} + \Delta v = V_{DC} + v_{rf}(cos\omega_1 t + cos\omega_2 t) \tag{4}$$

By substituting Eq. 4 in Eq. 3 we obtained a time-domain function of the modulation of the optical power. By applying a Fast Fourier Transform (FFT) on the obtained function, the $SFDR_{IMD_3}$ was extracted, for different applied voltages.

As previously shown in [27], linearity can be improved by increasing the junction doping levels. This is because highly doped p-n junctions show smaller depletion regions than low-doped junctions. As a result, the effective index modulation takes place within a more uniform optical mode distribution zone, thus the MZM transfer function could show an enhanced linearity

Table 1. MZM design: static simulation results. $v_{rf} = 4V$

	Loss [dB/mm]	Eff. [V.cm]	$SFDR_{IMD_3}$[dB $Hz^{2/3}$]	V_{bias}
Low (n=2.0$e17cm^{-3}$, p=4.0$e17cm^{-3}$)	0.36	1.92	74	1
	0.23	2.91	87	4
	0.14	4.07	89	8
Mid (n=2.7$e17cm^{-3}$, p=5.3$e17cm^{-3}$)	0.84	1.50	87	1
	0.62	2.09	91	4
	0.42	2.68	92	8
High (n=4.1$e17cm^{-3}$, p=8.0$e17cm^{-3}$)	1.35	1.37	93	1
	1.07	1.85	107	4
	0.83	2.37	109	8

with respect to an MZM equipped with low-doped p-n junctions, as phase shifters. On the other hand, changing the doping concentration also affects the loss coefficient as well as the modulation efficiency. We calculated the loss, efficiency and $SFDR_{IMD_3}$ for three different doping concentrations, thus selecting the most suitable configuration for our scope. The results are presented in Table 1.

By increasing the p-n junction doping concentration level, the $SFDR_{IMD_3}$ can be significantly improved, reaching a value of 109 dB $Hz^{2/3}$ for a high doping level, at a V_{bias} of 8 V. It is worth noting that, at this doping level, the efficiency is slightly improved with respect to the medium and low-doped junctions, showing also more uniform values for different bias voltages; it is also noted that, for high-doping levels, losses are only modestly increased, reaching a value of 1.07 dB/mm ($V_{bias} = 4V$). We identified the third configuration (high-doping level) as the most suitable for our targeted application.

2.2. Static characterization

Optical transfer functions for the MZM for different DC bias voltages applied to one of its electrodes are shown in Fig. 3. The induced phase shift ($\Delta\phi$) can be extracted by using the following equation:

$$\Delta\phi = \frac{2\pi\Delta\lambda}{FSR} \tag{5}$$

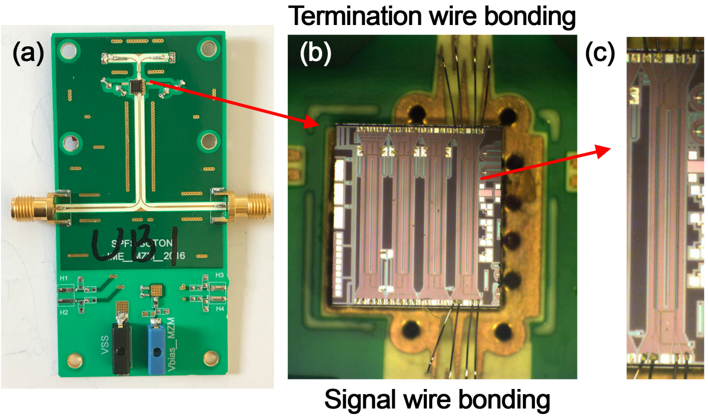

Fig. 2. (a) full device; (b) zoom of the optical unit and wire bonding and (c) zoom of the MZM optical unit.

where $\Delta\lambda$ is the wavelength shift measured on the nulls of the interference spectrum and FSR is the MZM Free Spectral Range. Measurements were carried out on both of the available phase shifters and results are reported in Fig. 3(b). The modulation efficiency $V_\pi L$ was assessed for different bias voltages by using the following equation [28–30]:

$$V_\pi L = \frac{\pi V_{bias} L}{\Delta\phi} \tag{6}$$

The obtained results, for different bias voltage values, for the two phase shifters, are shown in Fig. 3(c).

2.3. Electrical bandwidth analysis

Three sets of measurements were carried out to assess the impact of the electrical packaging on the MZM frequency response. The first characterization measured the electrical S21 parameter of the unpackaged MZM alone; the device was tested using high-speed RF probes that allowed to connect the device under test to a 50-GHz network analyzer. A -6.4 dB bandwidth of 26 GHz was measured when a DC bias voltage of 8 V was applied to the MZM phase shifter. A second set of electrical S21 measurements was carried out on the PCB board alone, which comprised just the RF microstrip lines (50 Ω) and two SMK-connectors, revealing a 10.02 GHz bandwidth. A final measurement was performed on the full packaged device, revealing a -6.4 dB bandwidth of 4.45 GHz on the electrical S21 parameter when the MZM was biased at 8 V. The measurements are reported in Fig. 4. The aim of these purely electrical measurements was to assess the impact of the electrical packaging on the electrical characteristics of the device. Besides, the electro-optical (E-O) MZM response could be affected by other effects (such as velocity mismatch between the optical and the electrical waves), eventually reducing the E-O device bandwidth. The significant bandwidth reduction observed on the packaged device shows that both the microstrip lines and the wire-bonding significantly deteriorated the electrical S21 parameter. The improvement of this aspect is the subject of further studies, and we are aiming at the adoption of more effective techniques, such as flip-chip bonding, in future device implementations. We show the E-O response of the packaged MZM device in Fig. 4(a), noting that only a slight mismatch is present between the 3-dB E-O bandwidth (4.33 GHz) and the -6.4 dB electrical bandwidth (4.45 GHz), suggesting that, in this case, the main limiting factor was the electrical packaging frequency response.

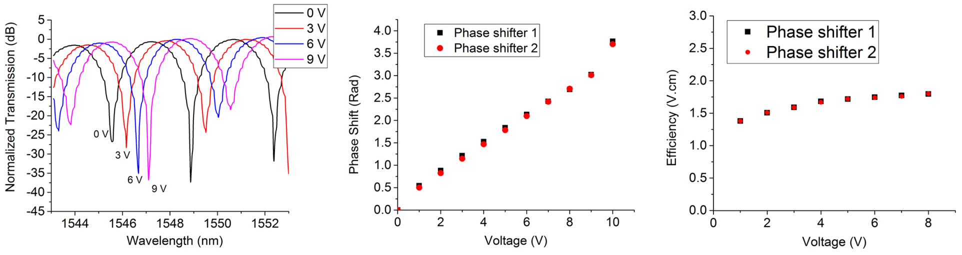

(a) (b) (c)

Fig. 3. (a) Normalized MZM optical transmission for different DC voltages applied to a single RF input port; (b) measured phase shift for a given applied voltage; (c) modulation efficiency measured for different bias voltages.

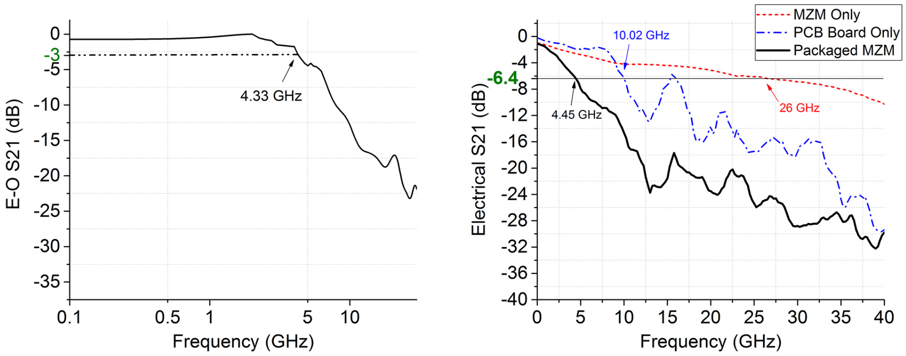

(a) (b)

Fig. 4. (a) E-O S21 parameter measured on the packaged device.(b) Electrical S21 parameter measured on the MZM device only (red dotted curve), the PCB board only (blue dash-dotted line) and the packaged MZM device (black line).

3. Linearity characterization

The performance of DMT-based optical systems has been shown to be strongly influenced by nonlinearities introduced by the transmission devices [31, 32]. Silicon MZMs are intrinsically nonlinear because of both the optical topology itself (the Mach-Zehnder interferometer) and the nonlinear nature of the carrier depletion effect [26] which is used as the modulation mechanism. The $SFDR$ is normally used to quantify the nonlinear behaviour of transmission components. When two input frequency tones are considered (f_1 and f_2) as the input to the MZM device, higher-order distortion components are created due to the device nonlinearity. The first two components are related to the second-order ($2f_1$ and $2f_2$) and third order distortions ($3f_1$ and $3f_2$), respectively. They also give rise to intermodulation components, these are second order ($f_1 + f_2$ and $f_2 - f_1$) and third order ($2f_2 - f_1$, $2f_1 - f_2$, $2f_2 + f_1$ and $2f_1 + f_2$) intermodulation distortions (IMD_2 and IMD_3, respectively). When a push-pull configuration is used, second order (and even higher order) terms are canceled out [33–35], therefore third order distortions are the main limiting factors in the system. It is also worth noting that third order intermodulation distortion components are always very close to the fundamental frequencies, therefore their impact has to be taken into account, even when a sub-octave bandwidth link is considered [35]. $SFDR_{IMD_3}$

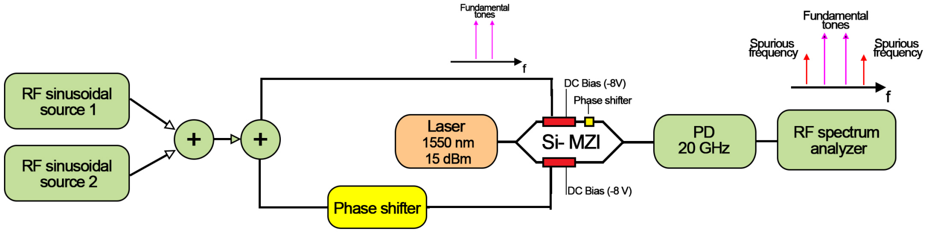

Fig. 5. Linearity measurement set-up.

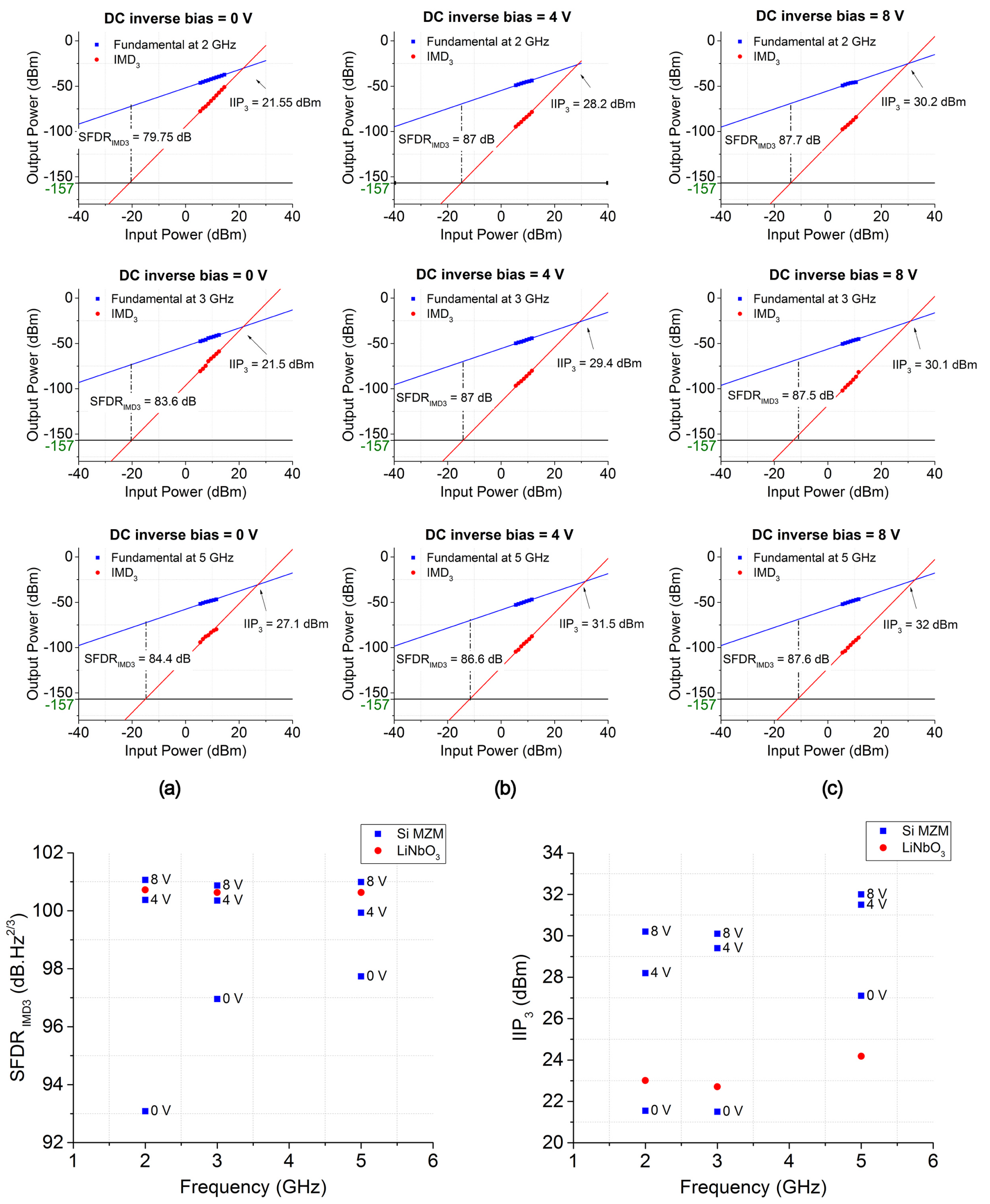

(d) (e)

Fig. 6. $SFDR_{IMD_3}$ measurements (resolution bandwidth $B = 100Hz$) carried out at a central frequency of 2,3 and 5 GHz on the Si-MZM biased at (a) 0 V, (b) 4 V and (c) 8 V; summary of (d) $SFDR_{IMD_3}$ (resolution bandwidth $B = 1Hz$) and (e) IIP_3 measurements. Blue squares represent measurements carried out on Si-MZM at different bias voltages, while the red points correspond to results obtained for the $LiNbO_3$ modulator, operated at the quadrature point ($V_{bias} = 2.1V$).

Table 2. Linearity of various Si-based modulators present in the literature.

	$SFDR_{IMD_3}$[dB $Hz^{2/3}$]	Central frequency [GHz]
[37] - Si- ring modulator	84	1
[38] - Si ring assisted MZM	99	10
[27] - Si MZM	113.7	2
[39] - Si ring assisted MZM	71.65	1
[40] - Si+III-V ring assisted MZM	117.5	10
[41] - Si MZM	95	1
[42] - Si MZM	97	1
This work Si-MZM	101	5

measurements were carried out using the experimental set-up shown in Fig. 5. A CW tunable laser provided the optical input signal at a fixed power level of 15 dBm. The light beam was transverse electrical (TE) polarized and launched in the silicon waveguide. The optical beam was collected at the output and sent to a 20-GHz linear photodiode which was connected to a RF spectrum analyzer. $SFDR_{IMD_3}$ was measured by using two sinusoidal tones mixed together in a 3-dB RF coupler and split to generate a pair of differential signals, which fed the MZM in push-pull mode. DC inverse bias was used in order to operate the MZM in depletion. Three different central frequency values were investigated, namely 2, 3 and 5 GHz adopting a tone separation of 0.01 GHz. The spectrum analyzer was used to measure the power levels of the two fundamental tones and the third intermodulation distortion signal using a resolution bandwidth B of 100 Hz on a background noise level of -157 dBm. In order to provide a context to this characterization, measurements were also carried out on a commercial 40-GHz $LiNbO_3$ modulator. Figure 6 (a)-(c) show $SFDR_{IMD_3}$ results for the Si MZM biased at 0, 4 and 8 V respectively, at three different central frequency values (2,3 and 5 GHz). Fig. 6(d) shows $SFDR_{IMD_3}$ measurements as a function of the central frequency and DC inverse bias voltage (on the Si MZM), normalized to a bandwidth resolution B value of 1 Hz [35], while Fig. 6(e) shows the third-order intermodulation intercept point (IIP_3) obtained for each SFDR measurement which represents the input power level at which the fundamental tones and the third order intermodulation tones are equal in power [36]. The $SFDR_{IMD_3}$ characterization demonstrated that our Si-MZM exhibits remarkable properties in terms of linearity, showing a $SFDR_{IMD_3}$ value of 101 dB $Hz^{2/3}$ and IIP_3 >30 dBm at 5 GHz frequency, when a reverse bias voltage of 8 V was adopted. We note that this measured value agrees considerably well to what expected from numerical simulations (see Tab. 1). In Table 2, we show $SFDR_{IMD_3}$ values, measured on Si- based modulators, previously reported in the literature.

4. DMT transmission experiments

The set-up we used for the DMT transmission experiments is shown in Fig. 7. The signal to be transmitted was generated off-line from a serial $2^{15} - 1$ Pseudo Random Bit Sequence (PRBS). The PRBS was sent to a serial-to-parallel block followed by a quadrature amplitude modulation (QAM) mapper which coded the bit-parallel sequence to constellation diagrams. The bit distribution across each constellation had been previously calculated using a rate adaptive water-filling algorithm [43, 44] which maximized the transmission bit-rate, for a given total energy, according to the response of our transmission channel. The algorithm we have used is described in detail in [43]. The transmission channel, had been characterized by sending a uniform QAM-modulated multi-carrier signal through the system. The complex conjugate of each mapped symbol was generated and then the entire sequence was transformed into a real-valued time sequence by means of an inverse fast Fourier transform (IFFT) block. A cyclic prefix (CP) was added (3.6%), followed by a parallel-to-serial block. An additional 2% preamble was added at each frame, for synchronization purposes. The resulting signal was then up-sampled and sent to a 32 GS/s Digital to Analog Converter (DAC) (bandwidth 20 GHz) which generated a pair of differential electrical signals. Two RF amplifiers (32 GHz bandwidth) were employed to boost the two signals providing a pair of 4 Vpp sequences which were used to drive the MZM (biased at 8 V inverse voltage). The optical carrier was provided by a pigtailed tuneable continuous wave (CW) laser which was coupled directly onto the MZM. The light beam was then transmitted through SMF spools with variable lengths ranging from 0 km (Back-To-Back - B2B) to 50 km. The receiver was composed of a noise loading block followed by a 30 GHz photodiode which converted the optical signal back to the electrical domain. The sequence was converted to a digital sequence using a 80 GS/s (35 GHz) analog-to-digital converter (ADC) and the resulting signal was stored and analyzed off-line. The signal was resampled and synchronized to determine the starting point of the DMT sequence and subsequently reconstructed as a parallel signal. After removing the CP, an FFT block was used to retrieve the QAM symbols which were de-mapped and equalized. A final parallel-to-serial operation allowed the received data to be obtained and compared to the transmitted data, in order to evaluate the bit-error ratio (BER).

The signal to noise ratio (SNR) channel response (40 km link) and the corresponding adopted bit loading diagram are shown in Fig. 8(a) and 8(b) respectively. 1342 symbols per frame were mapped across 239 sub-channels evenly distributed across a 10 GHz bandwidth reaching a transmission capacity of 52.42 Gb/s (frame transmission time of 25.6 ns). A net transmission rate of 49.6 Gb/s is achieved, after the CP and the 2 % of preamble sequence have been taken into account (see Tab. 3). 128-QAM was used as the highest constellation level. Both B2B and 40 km constellation diagrams (128-QAM and 64-QAM) are shown in Fig. 8(b). The measurements show that the linearity of the proposed MZM enabled the use of complex modulation formats without observing noticeable distortions, thus allowing to retrieve symbols, even when 128-QAM was used. For reference, the DMT parameters used in this experiment are also given in Tab. 3.

In order to evaluate the link performance, BERs were measured as a function of the SMF link reach (see Fig. 9). BER values below the 7% Hard Decision Forward Error Correction (HD-FEC)

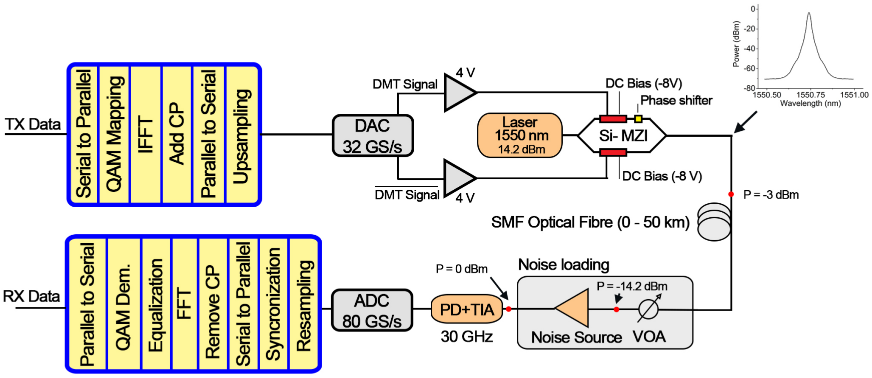

Fig. 7. DMT transmission set-up. QAM: Quadrature Amplitude Modulation; VOA: Variable Optical Attenuator; PD: Photodiode; TIA: Trans-impedance Amplifier; DAC: Digital to Analog Converter; ADC: Analog to Digital Converter.

Table 3. DMT parameters for 40 km-length link.

Number of channels (allocated)	FFT size	CP	Preamble	Sampling Rate
239	512	3.6 %	2 %	19 GS/s

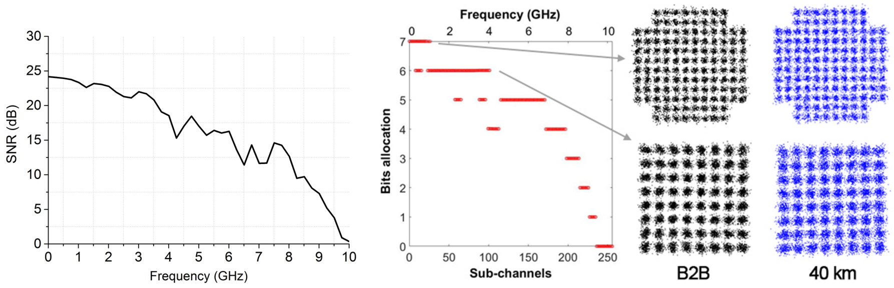

(a) (b)

Fig. 8. (a) Link-SNR measured after 40 km SMF propagation (b) bit loading results for 40 km-long transmission link. 128-QAM and 64- QAM constellation diagrams are shown for B2B and 40 km transmissions.

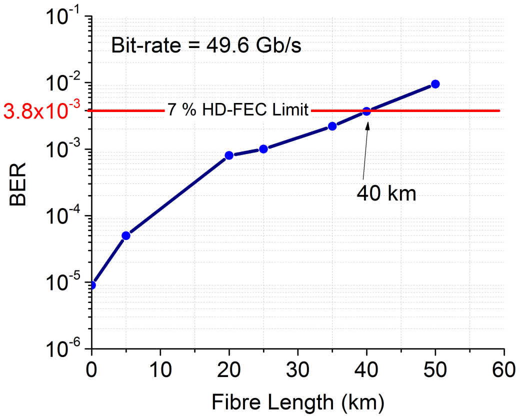

Fig. 9. BER measured for different SMF lengths. Note that for every BER result shown in this figure the OSNR was kept constant, thus the only impairment analyzed here is the CD.

limit were observed for SMF lengths in the range 0-40 km, while a BER of 10^{-2} was measured for a 50 km-long link. The main cause of BER degradation is the power fading effect due to the SMF chromatic dispersion (CD) which significantly affects the performance of Intensity Modulated (IM)-DD transmission links [45], introducing SNR penalties when relatively long fibres and/or high-frequency RF tones are used [46]. In an IM-DD link, the signal modulates both sides of the spectrum about the optical carrier. The phase relation between these two sidebands varies with the CD of the SMF, thus giving rise to distance-dependent signal distortions and manifesting itself as a power penalty at the receiver. The SNR penalty introduced by the fibre can be modelled using the following equation [45, 47]:

$$SNR_{penalty} = cos^2\left(\frac{\pi\lambda^2}{c} DLf^2\right) \tag{7}$$

where λ is the optical carrier central wavelength, D the fibre CD, L the fibre length and f the baseband tone frequency. We calculated the SNR penalties for three different SMF lengths with RF tones f spanning from 0 to 20 GHz. The results are shown in Fig. 10.

The grey zone in the graph indicates the bandwidth over which bits were allocated in our DMT

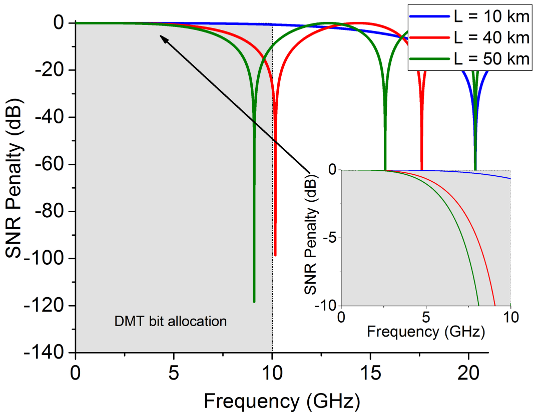

Fig. 10. SMF power fading SNR penalty calculated at a central wavelength of 1550 nm.

experiments. The blue curve relates to a 10 km-long SMF IM-DD link showing no SNR penalty for this signal bandwidth. The red curve was obtained for a 40 km length of SMF, exhibiting noticeable penalties at frequencies above 7 GHz, while the green line is for a 50 km-long SMF link, showing a further increase in SNR penalty. It is worth noting that the use of a modulator with a wider electrical bandwidth (e.g. >20 GHz) would only have a modest impact on the link performance at lengths >40 km, since high frequencies (> 10 GHz) would still be strongly affected by the SNR penalty, as shown in Fig. 10. The use of such high frequencies (f>10 GHz) would require bit allocation schemes of an increased complexity to finely discretize the system response, in order to precisely isolate tones where the CD power fading impact is prominent [18, 21]. The ability to utilise the available bandwidth effectively can be accounted for by the baseband spectral efficiency (SE), defined as the link net capacity divided by the signal bandwidth (in the electrical domain, baseband). In order to give context to our results, we report some baseband SE values for IM-DD systems already presented in the literature in Tab. 4, and compare them to the results achieved in this work. The optimal bit-allocation within the 10 GHz bandwidth (which does not suffer from CD power fading for lengths up to 40 km) and the high linearity behavior showed by our MZM which in turn allowed the use of dense modulation formats in the DMT coding (see Fig. 8) enabled us to transmit over 40 km of SMF exhibiting a baseband SE of 5 b/s/Hz, which is the

Table 4. Baseband SE for various transmission systems reported in literature.

	Format	Amplified	CD compensation	Length (km)	Baseband SE (b/s/Hz)	Rate(Gb/s)
Si-MZM with no electrical packaging [21]	DMT	No	No	10	4.4	107
Si-MZM with no electrical packaging [18]	DMT	No	No	4	3	90
Si-MZM with no electrical packaging [18]	SSB-DMT	No	No	40	2.8	100
Si-ring resonator with no electrical packaging [48]	PAM 4	Yes	No	20	1.33	40
Direct Modulated Laser (20 GHz E/O bandwidth) [34]	PAM 4	Yes	No	100	2.8	2 x 56
Direct Modulated Laser (15 GHz E/O bandwidth) [49]	DMT	No	No	80	2	49
Silicon photonic Stokes transmitter based on I/Q modulator [50]	16 QAM	Yes	Yes	100	6.4	128
Si-MZM I/Q Modulator with electrical packaging [22]	16 QAM	Yes	No	320	4	50
This work	DMT	No	No	40	5	49.6

highest value reported in the literature for silicon photonic DMT systems. Results shown in [18] and [21] use Si-MZM modulators exhibiting bandwidths >20 GHz but transmission lengths are limited to just 10 km due to the CD detrimental effect. SSB-DMT can be used to overcome this issue, as shown in [18, 22], but a more complex system is required to effectively suppress one sideband, making this choice less attractive for low-cost applications. Good performance is shown by PAM systems [34, 48] which are relatively simple and very attractive for data-center IM-DD systems, however the use of the available bandwidth is far from being optimised, since baseband SEs of 3 b/s/Hz are typically observed. A very high baseband SE transmission has been recently demonstrated in [50], reporting a 100 km transmission at 120 Gb/s data-rate; however, this system shows high complexity in both the transmitter and receiver side requiring an I/Q modulator, a Stokes receiver and a CD compensation block.

5. Conclusion

We demonstrated a silicon photonic IM-DD link based on DMT modulation operating at 49.6 Gb/s, transmitting over 40 km of SMF without the need of amplification and CD compensation. The DMT modulation was performed using a Si-MZM with electrical packaging, using 239 sub-carriers distributed over a 10 GHz bandwidth, obtaining a baseband SE of 5 b/s/Hz, which is the highest value reported in the literature to date for silicon photonic DMT-based systems.

Funding

National Natural Science Foundation of China (NSFC) (61535002, 61511130087); Engineering and Physical Sciences Research Council (EPSRC) (EP/L00044X/1).

Acknowledgments

This work was supported by EPSRC through the SPFS programme. X. Ruan and F. Zhang thank the support of National Natural Science Foundation of China (NSFC). Data available at http://dx.doi.org/10.5258/SOTON/20501340.